49th AIAA Aerospace Sciences Meeting including the New Horizons Forum and Aerospace Exposition
4 - 7 January 2011, Orlando, Florida

AIAA 2011-650

Simulations of High Speed Turbulent Jets in Crossflows

Xiaochuan Chai * and Krishnan Mahesh †
University of Minnesota, Minneapolis, MN, 55455, USA

Numerical simulations are used to study an under-expanded sonic jet injected into a supersonic crossflow and an over-expanded supersonic jet injected into a subsonic crossflow, where the flow conditions are based on Santiago *et al.*'s (1997) and Beresh *et al.*'s (2005) experiments, respectively. A finite volume compressible Navier–Stokes solver developed by Park & Mahesh (2007) for unstructured grids is used. The simulations successfully reproduce experimentally observed shock systems and flow vortical structures such as the barrel shock, Mach disk, horseshoe vortices that wrap up in front of the jet and the counter rotating vortex pair (CVP) downstream of the jet. The dynamics of these flow structures are discussed, as well as the effect of inflow turbulence. The time averaged flow fields are compared to the experimental results, and reasonable agreement is observed.

Nomenclature

J	=	Jet-to-crossflow momentum flux ratio
D	=	Jet diameter
R	=	Specific gas constant
M	=	Mach number
Re	=	Reynolds number
Pr	=	Prandtl number
μ	=	Viscosity
δ_{99}	=	Boundary layer thickness at 99% of freestream velocity
Subscript		
j	=	Quantities at jet exit
∞	=	Freestream quantities

I. Introduction

High speed jets in crossflows (JIC) have a variety of applications. For example, scramjet engines inject sonic under-expanded transverse jet of fuel into a supersonic crossflow of air. The efficient mixing of fuel and air is critical to the supersonic combustion. Accurate estimation and detailed physical understanding of the turbulent mixing mechanisms are important in combustor design. Supersonic jets are used for attitude or roll control on atmospheric flight vehicles. The supersonic jet plumes reorient upon encountering the crossflowing free stream and travel downstream where they can interact with aerodynamic control surfaces. In this case, understanding the turbulent characteristics in the far field of the jet is of great importance.

Sonic transverse jets in supersonic crossflows have been extensively studied. Experimentally, Santiago & Dutton[1] measured the detailed velocity distribution in the near field of a transverse jet; Gruber *et al.*[2] and VanLerberghe *et al.*[3] studied the time evolution of the flow fields and mixing characteristics of non-reactive

*Graduate Research Assistant, Department of Aerospace Engineering and Mechanics, AIAA student member.
†Professor, Department of Aerospace Engineering and Mechanics, 110 Union ST SE, AIAA Associate Fellow.

jets. Ben-Yakar *et al.*[4] studied reacting jets and jets with different molecular weights. These measurements showed the dynamics of the jet shear layer and shocks as well as the overall flow features. As observed by numerous studies,[2,4,5] the typical vortical structures of jet in crossflow include: (1) the near-field jet shear layer vortices; (2) the downstream wake vortices; (3) the horseshoe vortices wrapping around the jet column and (4) the counter-rotating vortex pair (CVP) in the far field. Figure 1 shows the presumed vortical structure for a transverse jet in a supersonic crossflow. On the numerical side, Peterson *et al.*[6] performed detached eddy simulations (DES) of a sonic jet in supersonic crossflows of two different Mach numbers and showed the presence of large-scale stuctures. Kawai and Lele[7–9] conducted implicit Large-eddy Simulations (LES) of a sonic jet into a Mach 1.6 supersonic crossflows. They investigated the velocity profiles at different locations downstream of the jet, the influence of laminar and turbulent inflow boundary layer, the time evolutions of shock system and turbulent eddy structures, as well as the mixing properties. Recently, Gènin and Menon[10] used LES to study the impact of the free stream Mach number and the jet-to-crossflow momentum ratio on the structure of the jet and the dynamics of jet-crossflow interaction.

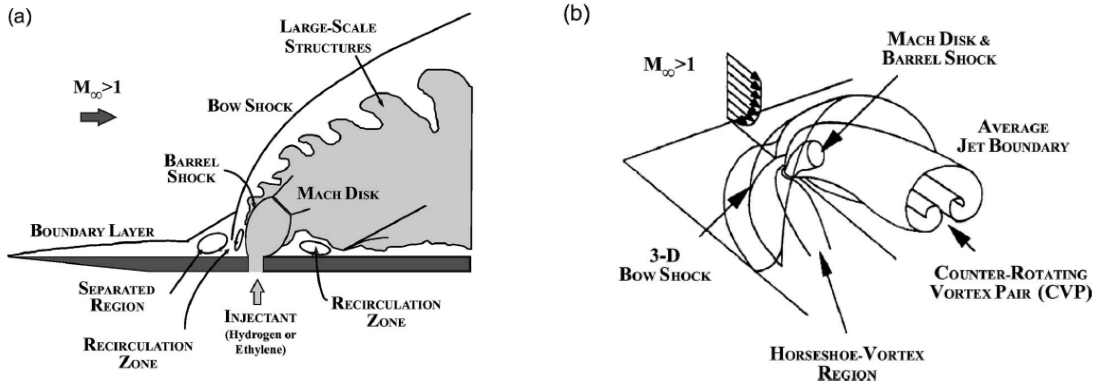

Figure 1. Schematic of an underexpanded transverse jet into a supersonic crossflow. (a) 2D view of vortex structures on central plane; (b) 3D perspective of averaged flow field. (images from Ref.[4,11])

Relatively fewer studies have been conducted on supersonic transverse jets in subsonic crossflows. Beresh *et al.*[12–14] carried out a series of experiments on over-expanded supersonic jets injected into subsonic crossflows. Based on 7 different flow configurations, Beresh *et al.* studied the influence of free stream Mach number and that of jet-to-crossflow momentum ratio on the penetration of the jet, the turbulent characteristics in the far field downstream of the jet and the scaling of counter-rotating vortex pairs (CVP) at cross planes.

Note that most previous simulations are performed on structured grids, and can not be extended to complex geometries. We are developing a novel unstructured grid methodology[15] for DNS/LES of high speed flows. Chai and Mahesh[16] simulated both a sonic transverse jet injected in a supersonic crossflow and a supersonic jet injected in a subsonic crossflow on unstructured grids, based on the experiments of Santiago *et al.*[1] and Beresh *et al*[12–14] respectively. The simulations were performed on relatively coarse grid, and used laminar boundary layer profiles as the boundary condition at the inflow. Reasonable agreement are observed between the simulation results and experimental data, which showed considerable promise of our unstructured Navier–Stokes solver to accurately reproduce these complex flows. In the present paper, we extend our simulations to finer grids and consider the realistic turbulent inflow boundary layer as well. The dynamics of the vortical structures and the shock systems are discussed. The time averaged flow fields are calculated and compared to the experimental results.

II. Simulation details

A. Numerical algorithm

The parallel, collocated finite volume solver for the compressible Navier–Stokes equations on unstructured grid developed by Park & Mahesh[15] is used. The algorithm solves the following governing equations:

$$\begin{aligned} \frac{\partial \rho}{\partial t} &= -\frac{\partial}{\partial x_j}\left(\rho u_j\right), \\ \frac{\partial \rho u_i}{\partial t} &= -\frac{\partial}{\partial x_j}\left(\rho u_i u_j + p\delta_{ij} - \sigma_{ij}\right), \\ \frac{\partial E_T}{\partial t} &= -\frac{\partial}{\partial x_j}\left\{\left(E_T + p\right) u_j - \sigma_{ij} u_i - Q_j\right\}, \\ p &= \rho R T \end{aligned} \tag{1}$$

Here, ρ, u_i, p and E_T are the density, velocity, pressure and total energy, respectively. R is the specific gas constant. The viscous stress σ_{ij} and heat flux Q_j are given by

$$\sigma_{ij} = \frac{\mu}{Re}\left(\frac{\partial u_i}{\partial x_j} + \frac{\partial u_j}{\partial x_i} - \frac{2}{3}\frac{\partial u_k}{\partial x_k}\delta_{ij}\right), \tag{2}$$

$$Q_j = \frac{\mu}{\left(\gamma - 1\right) M_\infty^2 Re Pr}\frac{\partial T}{\partial x_j} \tag{3}$$

after standard non-dimensionalization, where Re, M_∞ and Pr denote the Reynolds number, Mach number and Prandtl number. T is the temperature. And μ is the non-dimensionalized molecular viscosity which obeys Sutherland's viscosity law.[17]

Discretization of the governing equations involves reconstruction of the variables at the faces from the cell center values, and hence the spatial accuracy of the algorithm is sensitive to this flux reconstruction. Park & Mahesh[15] employ a modified least–square method for this reconstruction, which can be shown to be more accurate than a simple symmetric reconstruction, and more stable than a least–square reconstruction. In addition, the algorithm uses a novel shock–capturing scheme[15,18] based on a characteristic filter, which localizes the numerical dissipation to the vicinity of flow discontinuities – thereby minimizing unnecessary dissipation. Time–advancement of the solution is explicit. The algorithm is currently extended to the compressible dynamic Smagorinsky model[19] and dynamic k-equation model.[20] This paper reports results without the sub-grid scale model, so that the effect of the model can be assessed in future simulations.

B. Computational mesh and boundary conditions

Figure 2 shows the computational mesh and computational domain for the simulation of sonic jet in supersonic crossflow. The computational domain extends $40D \times 20D \times 30D$ in the axial, wall-normal and spanwise directions (x, y, and z) respectively. Preliminary computations show that a domain of this size is big enough to eliminate the effects of boundary conditions. No–slip and adiabatic boundary conditions are imposed on the walls of the flat plate and the nozzle. Zero–gradient boundary conditions are applied to the top, the two sides and the outflow. At the jet inlet, the experimental chamber pressure and density are specified so that the desired Mach number and thermodynamic conditions are achieved at the jet exit in absence of the crossflow. A *tanh* shape vertical velocity profile is imposed which satisfies the continuity and no–slip wall boundary condition. At the inlet of the crossflow, both laminar and turbulent boundary layer are considered. For laminar boundary layer, the similarity profiles of velocities and thermodynamic variables on a flat plate are prescribed at the inflow. For turbulent boundary layer, the inflow data is generated from a separate simulation of boundary layer transition (shown in figure 3). The inflow generator operates under the same flow conditions (Reynolds number and Mach number) as in the simulation of jet in crossflow. The inflow data are then extracted at a location where the boundary layer thickness matches the experimental

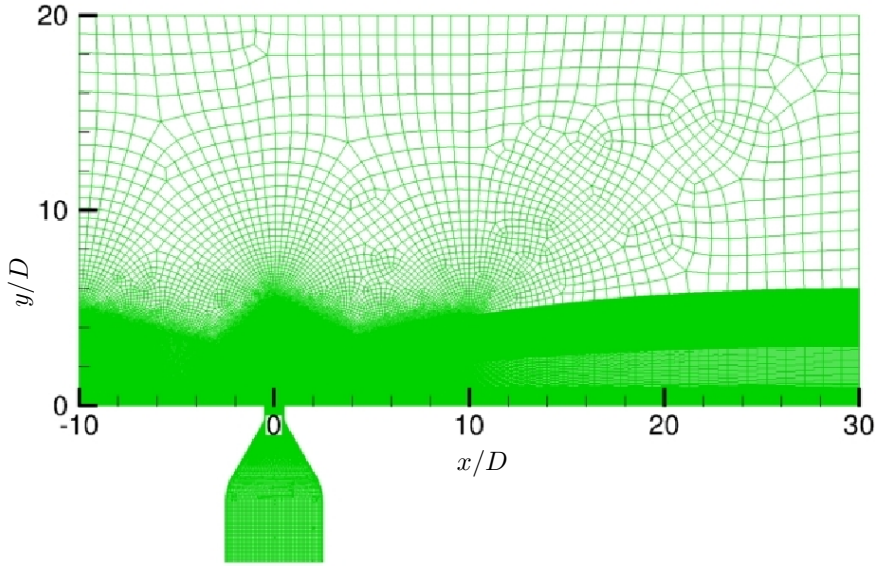

Figure 2. Computational mesh for sonic jet in supersonic crossflow.

condition and stored temporally. The stored inflow data is then read by the simulation of jet in crossflow. Figure 4 shows that the mean streamwise velocity profile of the inflow data is in good agreement with a fully developed turbulent boundary layer profile with a logarithmic region, and that the turbulent intensity profiles look reasonable.

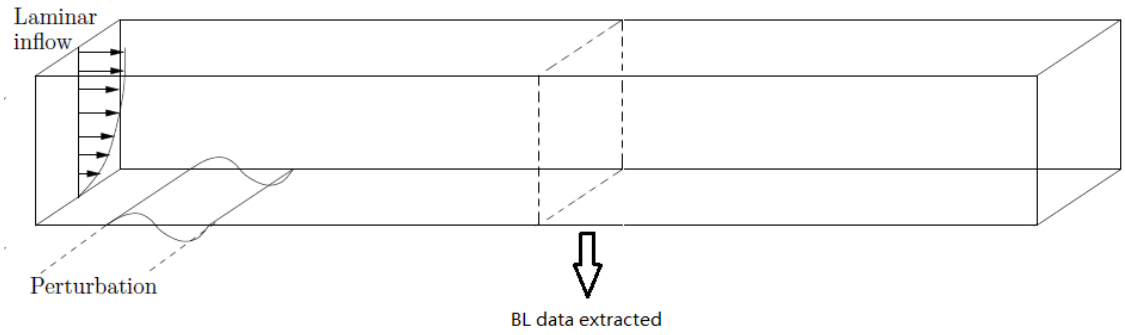

Figure 3. Schematic of turbulent inflow generator.

Figure 5 shows the computational mesh for the simulation of supersonic jet in subsonic crossflow. In this simulation, the penetration of the jet is 1/3 of the height of experimental apparatus. For comparison, the computational domain has almost the same dimension as the wind tunnel test section to account for the confinement effect of the wind tunnel walls. The computational domain extends $100d \times 32d \times 32d$ in the axial, wall-normal and spanwise directions respectively. Accordingly, adiabatic slip wall boundary conditions are specified for the sides and the top; while the boundary conditions for the walls of the flat plate and the nozzle, the jet inlet and the inflow are set similarly to those for sonic injection.

As shown in figure 2 and figure 5, the computational mesh is unstructured and consists of hexahedral elements only. Fine grids are used at critical regions such as the surface of the flat plate, the nozzle wall and the near field of the jet, etc. The grids are then stretched quickly outside of those regions. The meshes for laminar inflows have approximately 15 million control volumes. For turbulent inflows extra volumes

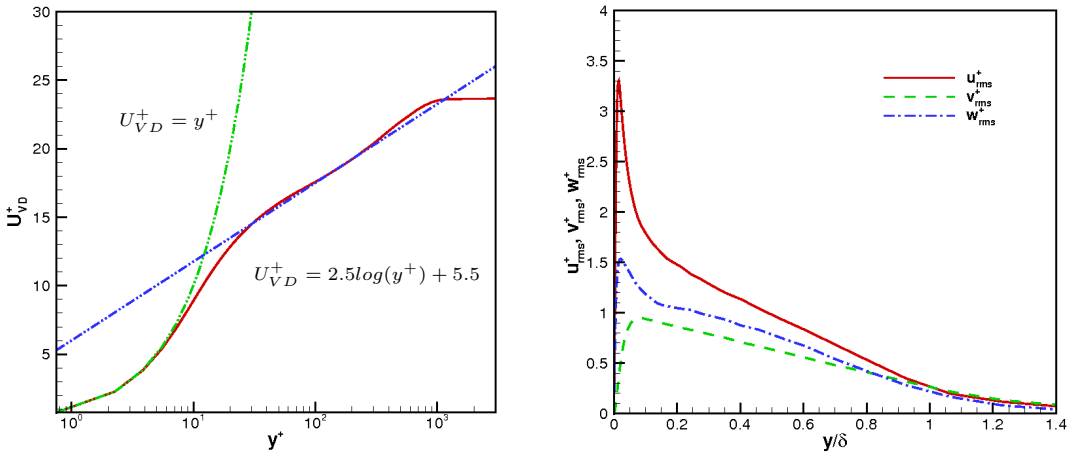

Figure 4. Mean velocity and turbulent intensity profiles of turbulent inflow boundary layer.

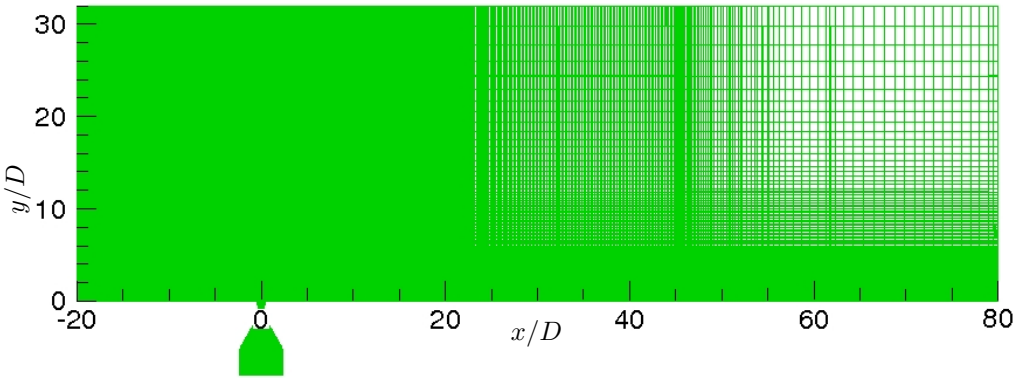

Figure 5. Computational mesh for supersonic jet in subsonic crossflow.

are required within the crossflow boundary layers to maintain the fully developed turbulence before its interaction with the jet. All statistics shown in this paper are obtained from a coarse grid simulation (25 million volumes); the instantaneous flow visualization in figure 6, 7 and 8 are obtained from a fine grid (60 million volumes) simulation in progress.

III. Sonic jet in supersonic crossflow

The flow condition examined here is based on the experiment of Santiago & Dutton,[1] where the free stream Mach number is $M_\infty = 1.6$ and the Reynolds number based on the free stream velocity and jet diameter D is $Re_D = 2.4 \times 10^5$. The density and pressure ratio between the nozzle chamber and crossflow are $\rho_{0j}/\rho_\infty = 5.5$ and $p_{0j}/p_\infty = 8.4$, resulting in a jet-to-crossflow momentum flux ratio of $J = 1.7$. The boundary layer thickness, $\delta_{99}/D = 0.775$ is matched at $x/D = -5$.

A. Instantaneous flow field

Figures 6 and 7 show the three–dimensional perspective of the instantaneous flow field at two different instants separated by one unit of time. Figure 7 shows contours of density gradient magnitude on the central plane and streamwise velocity contour on the horizontal plane, while figure 6 shows the density gradient

Figure 6. 3D view of instantaneous density gradient magnitude contours.

Figure 7. Contours of density gradient magnitude (central plane) and u velocity (horizontal plane).

magnitude contours on both planes. The crossflow travels from left to right and contains a fully developed turbulent boundary layer. The turbulent inflow encounters the transverse sonic jet and forms a bow shock, a recirculation region in front of the jet and a separation shock, followed by a decrease in streamwise velocity (Fig. 7). The recirculation region is highly unsteady and further induces a family of compression waves which interact with the bow shock. The crossflow fluid circumvents the jet and causes the separation bubbles to wrap around, which is marked by streaks on the sides of the jet (Fig. 6). Statistically these streaks correspond to the horseshoe vortices. Passing the jet, the crossflow accelerates as observed on the horizontal plane in figure 7. It is associated with the expansion of the incoming flow, which can be observed as the high density gradient magnitude region downstream of the jet on the horizontal plane of figure 6. The jet expands as it exits the nozzle and encounters the crossflow, forming inclined barrel shock and Mach disk. Strong shear layers are formed between the interface of the jet and crossflow. On the windward side of the jet, the shear layer rolls up into vortices which detach from the jet boundary and are shed downstream. By comparing the two instantaneous flow fields, it appears that the shedding of the shear layer vortices is accompanied by the deflections of the bow shock and that of the windward side of the barrel shock. The Mach disk changes its shape and location accordingly. On the leeward side, the lower pressure ambient fluid is entrained by the jet

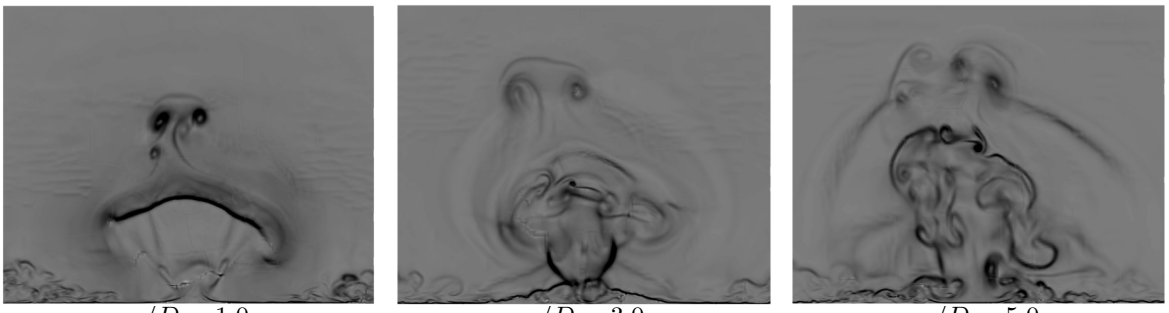

Figure 8. Instantaneous density gradient magnitude contours on the crossplanes at three downstream locations.

through the shear layer. The jet fluid that passes through the Mach disk experiences a sudden decrease of velocity magnitude, which induces two shear layers. One is the shear layer between the jet fluid that passes through the Mach disk and that passes through the windward side barrel shock; the other is between the jet fluid that passes through the Mach disk and the ambient crossflow fluid entrained by the leeward side shear layer. These shear layers break down quickly after the Mach disk due to the Kelvin-Helmholtz instability. Also observed are the wake vortices, and it is seen that there is an increase of turbulent length scale in the wake region.

Figure 8 shows the instantaneous density gradient contours on the crossplanes at three downstream locations. The 3D structures of those vortices mentioned above is clearly seen. Statistically, these vortices become counter-rotating vortex pair (CVP). However, the instantaneous field is rather unsteady.

B. Statistical results

Figure 9 compares the mean Mach number and mean streamwise velocity contours on the central plane between the simulations and the experiment. The shock system which includes the front bow shock, barrel shock, Mach disk, the separation shock in front of bow shock is clearly seen. Encountering the bow shock, the supersonic crossflow decelerates suddenly to subsonic, then expands and accelerates to supersonic again when it passes by the sonic jet. Recirculation regions are observed both upstream and downstream of the jet. The simulation results look similar to the experimental results qualitatively. However, a close observation shows that the contours predicted using turbulent inflow boundary layer are closer to the experiment's in terms of the shape, size, incline angle of the jet plume and the size of the recirculation region in front of the jet.

Quantitatively, velocity profiles are extracted at four different downstream locations on the central plane in figure 10. The simulation results show reasonable agreement with the experimental data, and using turbulent inflow improves the overall agreement. There are relatively big discrepancies near the wall in the near field of the jet. However, in Santiago *et al.*'s[1] paper, they note that their resolution in the near field downstream of the jet is inadequate for this flow, and they do not observe the downstream recirculation region. The downstream recirculation shown in figure 9 indicates that at locations $x/D = 1$ and $x/D = 2$ the near wall region should have downwash vertical velocity and a relatively smaller mean streamwise velocity, as shown in the velocity profiles in the simulations (Fig. 10). It is expected that the turbulent inflow boundary layer yields flatter slope of the streamwise velocity profile near the wall.

Figure 11 plots the streamwise velocity contours on the crossplanes at $x/D = 3$ and $x/D = 5$ downstream of the jet. Representative streamlines of in-plane velocities (v and w) are superimposed on the contours, which shows the counter rotating vortex pairs (CVP). Also shown are the pair of boundary layer separation vortices induced by the CVP and beneath the CVP. The coordinates of the CVP centers are estimated to be (0.60, 0.95) for laminar inflow case and (0.48, 1.10) for turbulent inflow at $x/D = 3$, and (0.62, 1.25) for laminar inflow and (0.60, 1.40) for turbulent inflow at $x/D = 5$, compared with the reported (0.50, 1.00) and (0.60, 1.40) at these two downstream locations in the experiment. The agreement between the simulations

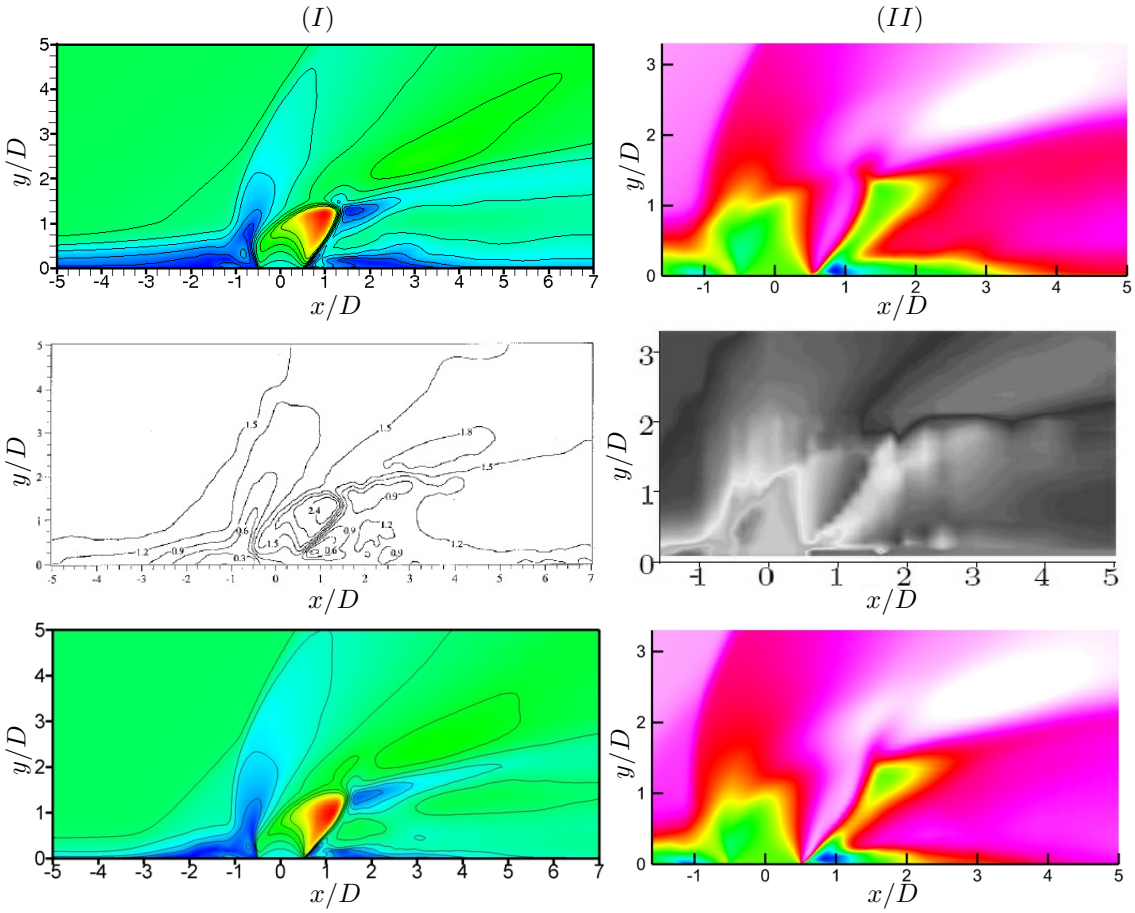

Figure 9. Time averaged Mach number contour (column I) and u velocity contour (column II) on central plane. First row, laminar inflow result; Second row, experiment; Third row, turbulent inflow.

and the experiment are reasonable, and the CVP center predicted using turbulent inflow are closer to the experiment in distance. Moreover, it appears that the u velocity contour for turbulent inflow spreads more than the laminar case, indicating an enhanced mixing due to the inflow turbulent boundary layer.

IV. Supersonic jet in subsonic crossflow

The simulation is based on Beresh's experiments,[12–14] where the free stream Mach number is $M_\infty = 0.8$; the nominal jet exit Mach number is $M_j = 3.73$; the jet-to-crossflow momentum ratio is $J = 10.2$; the density, pressure and temperature ratio between the nozzle chamber and crossflow are $\rho_{0j}/\rho_\infty = 47.1$, $p_{0j}/p_\infty = 49.1$ and $T_{0j}/T_\infty = 1.05$; The Reynolds number is $Re_D = 1.9 \times 10^5$ based on free stream conditions and the jet diameter D. The boundary layer thickness, $\delta_{99}/D = 1.553$ is matched at $x/D = 26.65$.

A. Instantaneous flow field

Figure 12 shows the iso-surface of the second invariant of velocity gradient tensor, which visualizes the vortical structures within this flow. Similar to the sonic injection, the crossflow boundary layer travels from left to right. The turbulent inflow encounters the transverse supersonic jet, forming a recirculation region in front of the jet. The separation bubbles wrap around the jet and stretch along the streamwise direction, forming the horseshoe vortices, which are marked by the high Ω_x magnitude stipes (dark blue and red) on the sides of the jet in figure 12. Note that the jet penetrates a lot more than the sonic jet due to much

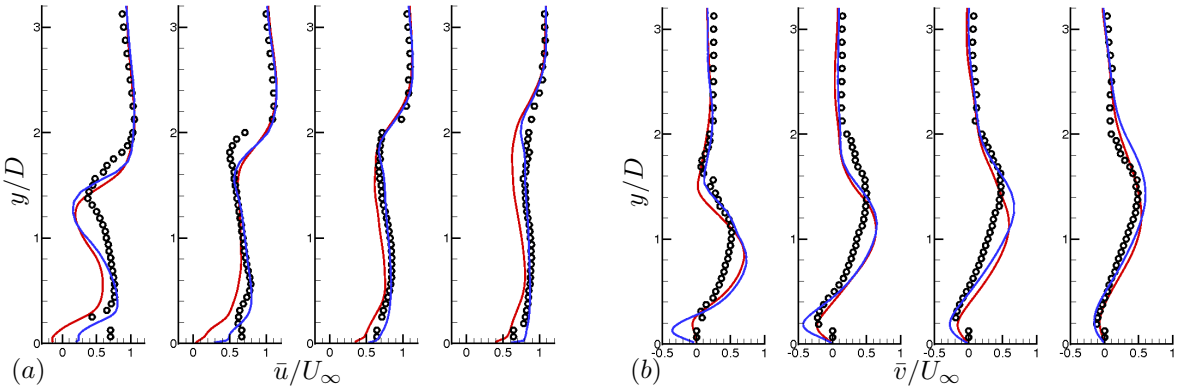

Figure 10. Comparisons of streamwise (a) and wall-normal (b) velocities between simulation and experiment at jet downstream locations $x/D = 2, 3, 4, 5$. Red lines = simulation using laminar inflow; Blue lines = simulation using turbulent inflow; Symbols = experiment.

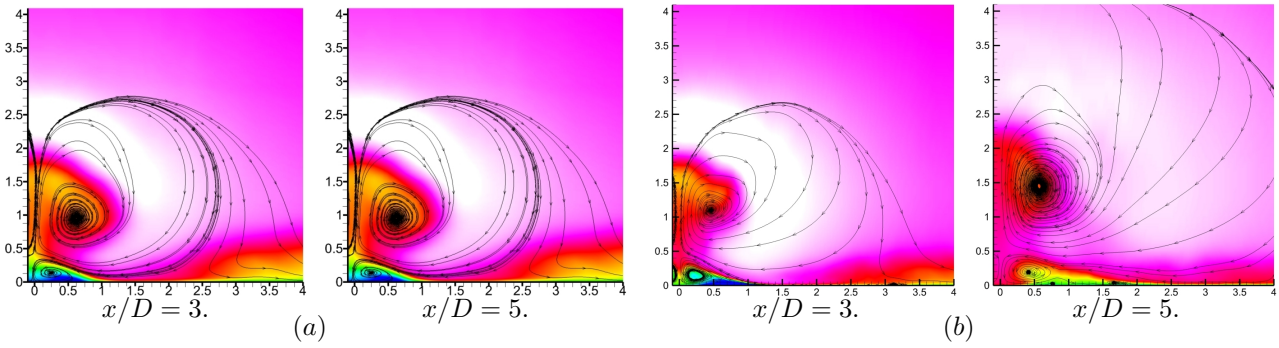

Figure 11. v–w streamlines superimposed on the streamwise velocity contour on crossplanes at $x/D = 3$ and $x/D = 5$. a) Laminar inflow boundary condition; b) turbulent boundary condition.

higher jet-to-crossflow momentum ratio. The shear layer vortices roll up on the windward side of the jet grow and travel along with the jet, instead of shedding downstream. These shear layer vortices have ring-type structures surrounding the jet plume. Looking along the streamwise direction, the left hand side and the right hand side of the jet plume have different signs of Ω_x. Statistically, these become the counter-rotating vortex pairs. The wake vortices which originate from separation of the crossflow boundary layer, according to Fric *et al.*'s work,[5] are clearly seen. The turbulent length scale increases within the wake.

Figure 13 compares the instantaneous Mach number contour on the central plane between simulation results using laminar inflow and turbulent inflow. In front of the jet, the flow field looks like an incompressible jet in crossflow in that no bow shock and separation shock are formed because the crossflow is subsonic. The crossflow is retarded by the injected jet fluid, forming strong back pressure on the windward side of the jet which causes the separation of crossflow boundary layer. At the jet exit, the barrel shock and Mach disk are clearly observed. The jet accelerates within the barrel shock, bends and decelerates as it passes through the barrel shock and Mach disk. Shock cells are seen within the jet plume, where the jet fluid get expanded and compressed alternately, causing the jet boundary expands and contracts accordingly. Also shown is the strong jet-crossflow shear layer, which rolls up into vortices and causes the deflections of jet boundaries at the windward side of the jet. The streamlines of the in plane velocities are used to show the recirculation region in front of the jet. It shows that the recirculation region are smaller and closer to the jet in the simulation using turbulent inflow. It also appears that with turbulent inflow there are more fine flow structures downstream of the jet.

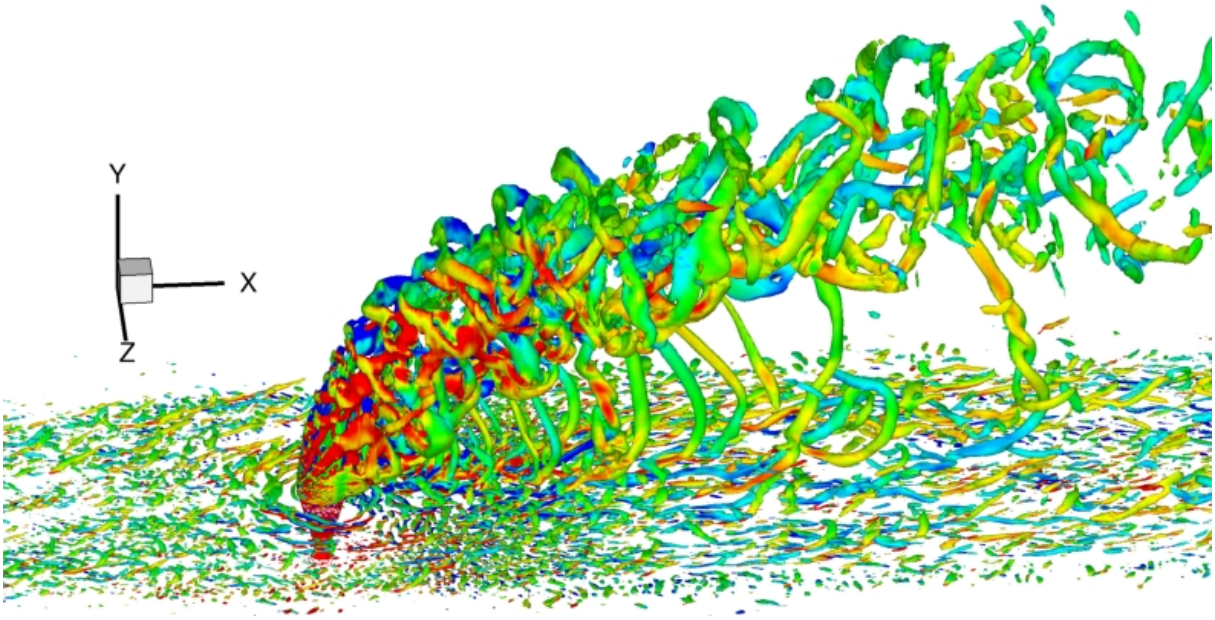

Figure 12. Iso-surface of the second invariant of velocity gradient tensor Q colored by streamwise vorticity Ω_x.

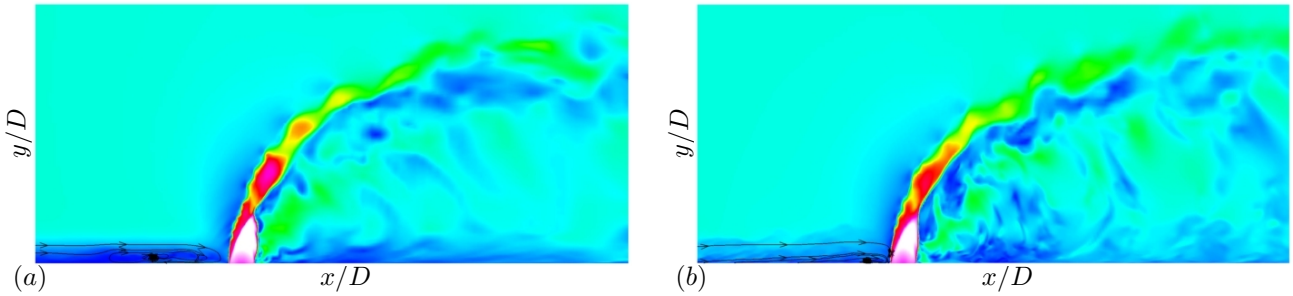

Figure 13. Instantaneous Mach number contours on the central plane. (a) Laminar inflow; (b) Turbulent inflow.

B. Statistical results

Figure 14 compares the time averaged streamwise and vertical velocity field with the experimental results. The vertical velocity fields predicted by the simulations show very good agreement with the experiment. In the simulation with laminar inflow, the low u–velocity region spreads more than the experiment, blurring the trajectory of minimum u–velocity. Using turbulent inflow improves this distribution of u–velocity and the agreement with experiment.

Quantitatively, the mean velocity profiles are extracted at five different locations downstream of the jet, shown in figure 15. The peak of the u–velocity deficit indicates the location of the jet core which has the largest impedance to the oncoming crossflow, while the peak of v–velocity marks the position of the CVP which induces the v–velocity component. Both peaks are measures of the jet trajectory. Consistent with figure 14, the peak of the streamwise velocity deficit using laminar inflow spreads wider than the experiment result in each profile, which is improved by using turbulent inflow, especially in the far field. Using turbulent inflow boundary layer also shows noticeable improvement at the near wall region and the overall agreement. In terms of the vertical velocity, the simulation using turbulent inflow shows very good agreement with the experiment, while using laminar inflow over-predicts the trajectory of the jet. This is reasonable, because

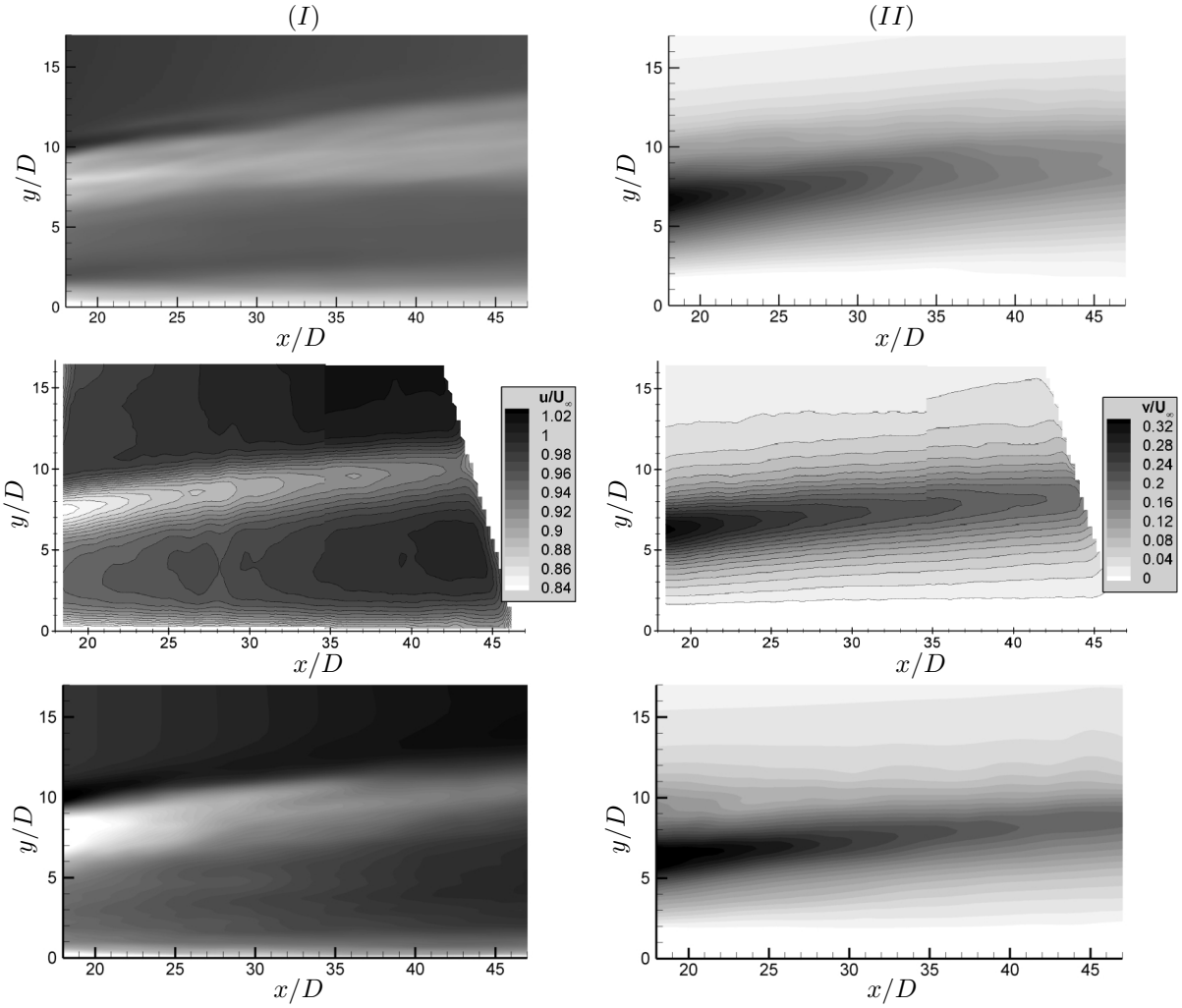

Figure 14. Time averaged u velocity contour (column I) and v velocity contour (column II) on central plane. First row, laminar inflow; Second row, experiment; Third row, turbulent inflow.

the laminar boundary layer has less momentum near the wall, which make it easier to be penetrated.

V. Conclusions

Numerical simulations of an under-expanded sonic jet in a supersonic crossflow and a supersonic jet in a subsonic crossflow are performed to study the key physics of high speed jets in crossflows. The parallel finite volume Navier-Stokes solver on unstructured grids developed by Park & Mahesh[15] is used. Common flow structures in the two cases include the barrel shock and the Mach disk, the separation region of inflow boundary layer in front of the jet, unsteady jet-crossflow shear layer and counter rotating vortex pair. The separation bubbles wrap around the jet and are elongated by the crossflow, forming horseshoe vortices. Increase of turbulent length scales is noticed within the downstream boundary layer. In the sonic injection, a bow shock and a separation shock are formed in front of the jet due to the supersonic crossflow. In the simulation of supersonic jet in subsonic crossflow, the jet penetrates more into the crossflow due to high momentum ratio. Shock cells are observed within the supersonic jet, causing the jet to expand and contract alternately. The cylinder like wake vortices are clearly visualized.

The effects of turbulent inflow boundary layer are studied and found to be significant to the simulation

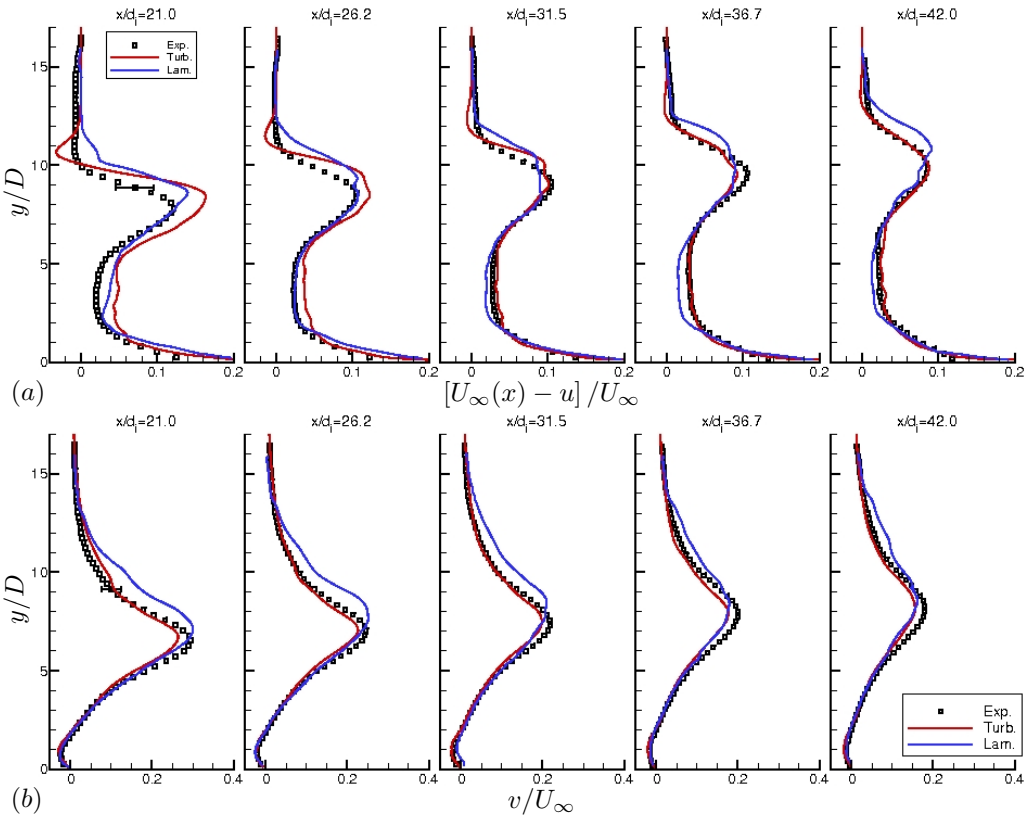

Figure 15. Comparisons of streamwise velocity deficit (a) **and wall-normal velocity** (b) **between simulation and experiment at jet downstream locations x/D = 21, 26.2, 31.5, 36.7, 42.0. lines = simulations, symbols = experiment.**

results. Using turbulent inflow boundary layer improves the agreement in the statistical results between the simulations and the experiments. Turbulent boundary layers have more momentum near the wall, therefore postpone the separation of the free stream boundary layer, which makes the recirculation regions to be smaller and closer to the jet. For the same reason, using turbulent inflow in the supersonic injection predicts more accurate jet penetration which is over-predicted in laminar inflow simulation. In sonic injection, the influence on the penetration is small, but it appears that the mixing of the jet and crossflow is enhanced by the turbulent inflow boundary layer.

Time averaged flow fields are computed, as well as the mean velocity profiles. Reasonable agreement is observed between available simulations and experimental data for both cases. The presented work shows the considerable promise of our unstructured algorithm to accurately reproduce these complex flows.

Acknowledgments

This work is supported by the National Science Foundation under grant CTS-0828162. Computer time for the simulations was provided by Minnesota Supercomputing Institute (MSI), National Institute for Computational Sciences (NICS) and Texas Advanced Computing Center (TACC). We thank Prof. Santiago and Dr. Beresh for providing data from their experimental studies, and Dr. Suman Muppidi for several useful discussions.

References

[1]Santiago, J. G., and Dutton, J. C., Velocity Measurements of a Jet Injected into a Supersonic Crossflow, *Journal of Propulsion and Power*, Vol. 13, No. 2, 1997, pp. 264–273.

[2]Gruber, M.R., Nejad, A.S., Chen, T.H., Dutton, J.C., Large structure convection velocity measurements in compressible transvers injection flow-fields, *Exp. Fluids*, Vol. 12, No.5, 1997, pp. 397–407.

[3]VanLerberghe, W. M., Santiago, J. G., Dutton, J. C. & Lucht, R. P., Mixing of a sonic transverse jet injected into a supersonic flow, *AIAA Journal*, Vol. 38, No. 3, 2000, pp. 470–479.

[4]Ben-Yakar, A., Mungal, M.G., Hanson, R.K., Time evolution and mixing characteristics of hydrogen and ethylene transverse jets in supersonic crossflows, *Physics of Fluids*, Vol. 18, No. 2, Feb 2006.

[5]Fric, T. F., and Roshko, A., Vortical structure in the wake of a transverse Jet, *Journal of Fluid Mechanics*, Vol. 279, pp. 1–47, 1994.

[6]Peterson, D.M., Subbareddy, P.K., Candler, G.V., Assessment of synthetic inflow generation for simuating injection into a supersonic crossflow, *AIAA Paper*, 2006-8128.

[7]Kawai, S. and Lele, S. K., Mechanisms of jet mixing in a supersonic crossflow: a study using large-eddy simulation, *Center for Turbulence Research Annual Research Briefs*, 2007.

[8]Kawai, S. and Lele, S. K., Large-eddy simulation of jet mixing in a supersonic turbulent crossflow, *Center for Turbulence Research Annual Research Briefs*, 2008.

[9]Kawai, S. and Lele, S. K., Dynamics and mixing of a sonic jet in a supersonic turbulent crossflow, *Center for Turbulence Research Annual Research Briefs*, 2009.

[10]Génin., F., Menon., S., 2010, Dynamics of sonic jet injectiion into supersonic crossflow, *J. Turbulence*, 11:1–13

[11]Gruber, M.R., Nejad, A.S., Chen, T.H., Dutton, J.C., Compressibility effects in supersonic transverse injection flowfields, *Physics of Fluids*, Vol. 9, No. 5, May 1997.

[12]Beresh, S. J., Henfling, J. F., Erven, R. J., and Spillers, R. W., Penetration of a Transverse Supersonic Jet into a Subsonic Compressible Crossflow, *AIAA Journal*, Vol. 43, No. 2, 2005, pp. 379–389.

[13]Beresh, S. J., Henfling, J. F., Erven, R. J., and Spillers, R. W., Turbulent Characteristics of a Transverse Supersonic Jet in a Subsonic Compressible Crossflow, *AIAA Journal*, Vol. 43, No. 11, 2005, pp. 2385–2394.

[14]Beresh, S. J., Henfling, J. F., Erven, R. J., and Spillers, R. W., Crossplane Velocimetry of a Transverse Supersonic Jet in a Transonic Crossflow, *AIAA Journal*, Vol. 44, No. 12, 2006, pp. 3051–3061.

[15]Park, N. and Mahesh, K. 2007, Numerical and modeling issues in LES of compressible turbulent flows on unstructured grids, *AIAA Paper*–722.

[16]Chai, X., Mahesh, K., 2010, Simulations of High Speed Turbulent Jets in Crossflow, *AIAA paper* 2010-4603.

[17]Sutherland, W. , The viscosity of gases and molecular force, *Philosophical Magazine* S. 5, 36, pp. 507-531, 1893.

[18]Yee, H. C., Sandham, N. D., and Djomehri, M. J. Low-dissipative high-order shock-capturing methods using characteristic-based filters, *J. of Comput. Phys.*–**150**:199, 1999.

[19]Moin, P., Squires, K., Cabot, W. and Lee, S., 1991, A dynamic subgrid-scale model for compressible turbulence and scalar transport, *Phys. Fluids A* **3**: 2746.

[20]Chai, X., Mahesh, K., 2010, Dynamic k-Equation Model for Large Eddy Simulation of Compressible Flows, *AIAA paper* 2010-5026.